



Cite as
Nano-Micro Lett.
(2020) 12:177

Received: 15 May 2020
Accepted: 4 August 2020
Published online: 29 August 2020
© The Author(s) 2020

An Efficient Trap Passivator for Perovskite Solar Cells: Poly(propylene glycol) bis(2-aminopropyl ether)

Ningli Chen^{1,2}, Xiaohui Yi^{1,3}, Jing Zhuang^{1,2}, Yuanzhi Wei^{1,2}, Yanyan Zhang⁴, Fuyi Wang^{2,4}, Shaokui Cao⁵, Cheng Li³, Jizheng Wang^{1,2} ✉

✉ Jizheng Wang, jizheng@iccas.ac.cn

¹ CAS Key Laboratory of Organic Solids, Beijing National Laboratory for Molecular Sciences, Institute of Chemistry Chinese Academy of Sciences, Beijing 100190, People's Republic of China

² University of Chinese Academy of Sciences, Beijing 100190, People's Republic of China

³ Department of Physics, Xiamen University, Xiamen 361005, People's Republic of China

⁴ CAS Key Laboratory of Analytical Chemistry for Living Biosystems, Beijing National Laboratory for Molecular Sciences, Institute of Chemistry Chinese Academy of Sciences, Beijing 100190, People's Republic of China

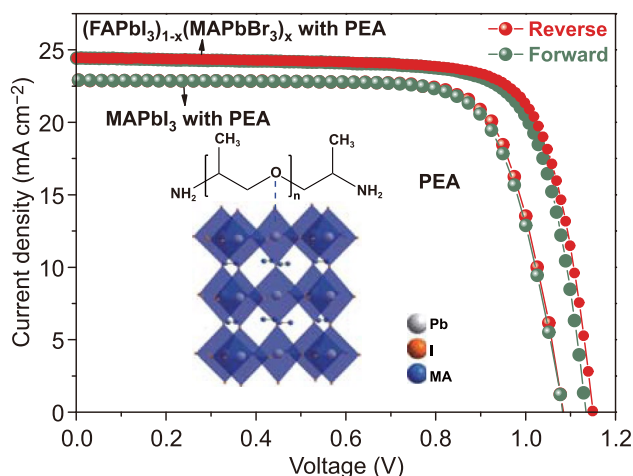
⁵ School of Materials Science and Engineering, Zhengzhou University, Zhengzhou 450000, People's Republic of China

HIGHLIGHTS

- Poly(propylene glycol) bis(2-aminopropyl ether) (PEA) additive is introduced into the perovskite solar cells to passivate both surface and grain boundary defects, and hence improve the device efficiency and stability.
- MAPbI₃ device with PEA exhibits significantly enhanced efficiency of 18.87%. (FAPbI₃)_{1-x}(MAPbBr₃)_x device with PEA exhibits enhanced efficiency of 21.60%.
- The unsealed passivated device degrades only by 5% in PCE after being exposed to air (30 ± 5% relative humidity) for 30 days.

ABSTRACT Perovskite solar cells (PSCs) are regarded as promising candidates for future renewable energy production. High-density defects in the perovskite films, however, lead to unsatisfactory device performances. Here, poly(propylene glycol) bis(2-aminopropyl ether) (PEA) additive is utilized to passivate the trap states in perovskite. The PEA molecules chemically interact with lead ions in perovskite, considerably passivate surface and bulk defects, which is in favor of charge transfer and extraction. Furthermore, the PEA additive can efficiently block moisture and oxygen to prolong the device lifetime. As a result, PEA-treated MAPbI₃ (MA: CH₃NH₂) solar cells show increased power conversion efficiency (PCE) (from 17.18 to 18.87%) and good long-term stability. When PEA is introduced to (FAPbI₃)_{1-x}(MAPbBr₃)_x (FA: HC(NH₂)₂) solar cells, the PCE is enhanced from 19.66 to 21.60%. For both perovskites, their severe device hysteresis is efficiently relieved by PEA.

KEYWORDS Defects; Grain boundaries; Passivation; Stability; Perovskite solar cells



1 Introduction

Perovskite solar cells (PSCs) are attractive as next-generation photovoltaic devices due to their outstanding properties such as easy preparation, low cost, and high efficiency [1–5]. PSCs are first reported in 2009 [6], and since then, rapid progress has been made in improving their performances. Recently, a certified power conversion efficiency (PCE) of exceeding 25% has been reported [7], reaching those of crystalline silicon solar cells [8]. However, a general and lasting problem for PSCs is that the perovskite films has abundant defects, at either surface or grain boundaries (GBs) [9]. These defects not only serve as recombination centers (to reduce carrier lifetime and charge extraction efficiency) [10, 11], but also facilitate the permeation of moisture and oxygen into the perovskite film, which seriously accelerates the device degradation [12–14]. Thus, defect passivation is highly desirable for achieving PSCs with both high PCE and high stability.

Surface passivation by coating molecules containing passivation groups on the surface of the perovskite layer has been proven successful for the enhancement of the device efficiency and durability. For example, the benzylamine-modified FAPbI₃ (FA: HC(NH₂)₂) solar cells exhibit a champion efficiency of 19.2% and prolonged moisture durability over 2900 h [15]. By adopting a poly(methyl methacrylate) polymer layer on the MAPbI₃ film, the device stability in moisture air is largely enhanced [16].

GB passivation via introducing additives, such as metal ions [17], small organic molecules [18, 19], polymers [20, 21], and polymer-small molecules mixtures [22], in the perovskite layer, has been a route on improving the device performance. Among these additives, polymers preferentially incorporate between GBs due to their large sizes, are able to form stable and reliable interactions with perovskite grains [23], and hence have attracted significant research interest. Zuo et al. employed poly(4-vinylpyridine) in MAPbI₃, improved PCEs from 16.9 ± 0.7 to 18.8 ± 0.8% and gained prolonged shelf lifetime of up to 90 days [23]. Qin et al. reported that introducing polymer PBDB-T into (CsPbI₃)_{0.04}(FAPbI₃)_{0.82}(MAPbBr₃)_{0.14} leads to passivation of GBs. Consequently, the device shows an improved PCE of 19.85%, and is able to retain about 90% of the initial PCE after 150 days [24].

In this study, we use poly(propylene glycol) bis(2-aminopropyl ether) (PEA), which contains rich ether-oxygen groups, for the perovskite surface and GB defect passivation. The PEA molecules existing at perovskite GBs and surface chemically interact with Pb ions, retarding trap-related nonradiative recombination and enhancing charge transfer and extraction. As a result, an improvement of PCE from 17.18 to 18.87% for MAPbI₃ solar cells is observed. Moreover, the hydrophobic PEA molecules at GBs and surface can efficiently block moisture, which significantly strengthens the device stability in air. Without any encapsulation, the MAPbI₃ device with PEA maintains 95% of its original PCE after 30 days. The PEA-incorporated (FAPbI₃)_{1-x}(MAPbBr₃)_x solar cells achieve an improved PCE from 19.66 to 21.60%. For both perovskites, PEA efficiently eliminates their original serious device hysteresis.

2 Results and Discussion

2.1 Characterization of MAPbI₃ Films and Devices with PEA

The chemical structure of a PEA molecule is shown in Fig. 1a. Pb²⁺ ions in perovskite have 6p empty electron orbits. The lone electron pairs from ether-oxygen in PEA can be delocalized to the empty orbits of Pb²⁺, forming coordination bonds [23, 25, 26]. The ether-oxygen unshared electron pair activates to form a crosslinking complex with lead ions at perovskite surface and GBs. As a result, the defect density is effectively decreased and the non-radiative recombination of the perovskite film is much inhibited [27]. This interaction is validated by Fourier transform Infrared (FTIR) spectra and X-ray photoelectron spectroscopy (XPS) measurements. Figure S1 displays the FITR spectra of PEA and the MAPbI₃ films without (the control film) and with 1 wt% PEA. The PEA features a peak at 1110 cm⁻¹, corresponding to the C–O–C stretching mode. The C–O–C peak shifts to a lower wavelength of 1064 cm⁻¹ for the MAPbI₃ film with PEA, and this is caused by the PEA molecule–perovskite interaction [28, 29]. This interaction is further verified by performing XPS measurements on the MAPbI₃ films with and without PEA. The overview spectra are shown

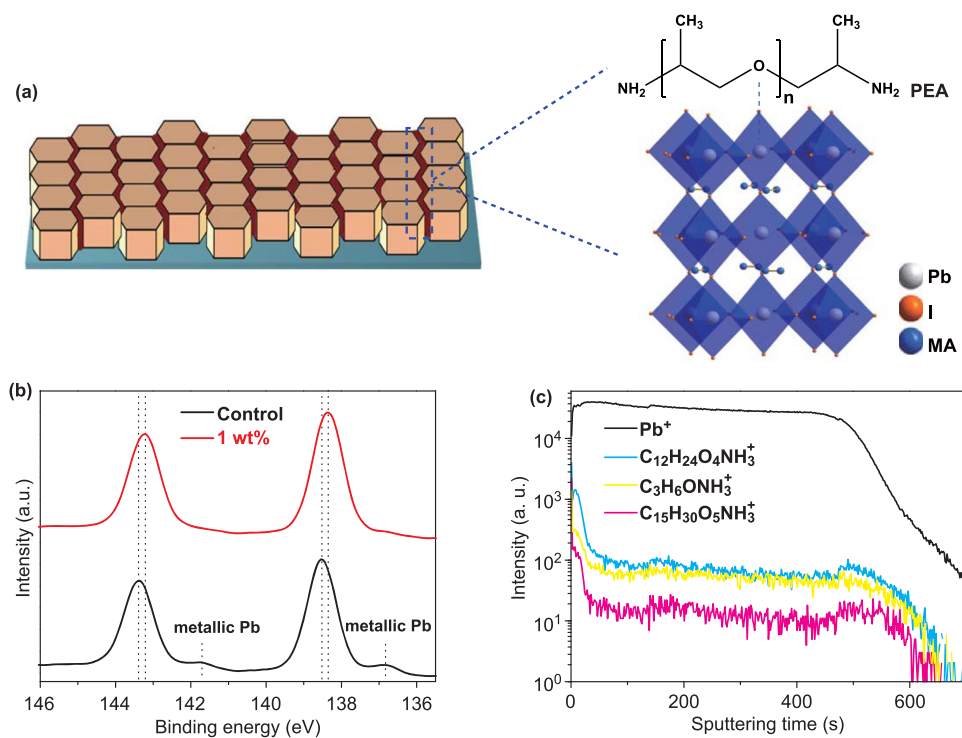


Fig. 1 **a** Schematic diagram of the GB passivation. **b** XPS spectra of Pb 4f for the MAPbI₃ films with and without PEA, and **c** SIMS profiles showing Pb and PEA elements from the top to the bottom of the MAPbI₃ film with PEA

in Fig. S2 (the binding energy scale calibration has been done by measuring the Au 4f peak at 84.0 eV). The C 1s, N 1s, I 3d, O 1s spectra are shown in Fig. S3. The C 1s spectrum of the MAPbI₃ film is fitted with several peaks of 285.0, 285.7, and 286.5 eV, which can be attributed to CH₃I, surface adsorbed oxygen, and C–N bonds [19, 30]. For the C 1s spectrum of the MAPbI₃ film with PEA, a new peak at about 287 eV appears, which can be attributed to C–O bonds in PEA [31]. And, the relative content of C–N bonds increases when PEA is presented (PEA also contains C–N bonds). The Pb 4f spectra are shown in Fig. 1b. The binding energy of Pb 4f_{7/2} (4f_{5/2}) shifts from 138.52 (143.39) to 138.35 (143.21) eV. This shift confirms the decrease in cationic charge of Pb²⁺ ions in MAPbI₃, which could be ascribed to the donation of a lone electron pair in PEA to the 6p empty orbits of Pb²⁺ [32–35]. Moreover, there are two small peaks at 136.86 and 141.75 eV in the Pb 4f spectrum of the control MAPbI₃ film, which could be associated with the existence of metallic Pb [36]. The metallic Pb defects act as nonradiative recombination centers [37], hindering

carrier transfer and collection. After PEA is added, these two small peaks diminish, implying the passivation of these defects. To study the PEA distribution throughout the MAPbI₃ film with PEA, time-of-flight secondary-ion mass spectrometry (TOF–SIMS) tests were conducted. The “Pb⁺” from MAPbI₃, “(C₃H₆O)_nNH₃⁺” from PEA are tracked (Fig. 1c). It is found that (C₃H₆O)_nNH₃⁺ appear at the surface of the MAPbI₃ film and exhibit a uniform distribution in the bulk film. Furthermore, due to the large size of the polymer, there is no opportunity for the PEA molecules to incorporate into the perovskite lattice. They would mainly accumulate in the gaps between GBs [29, 38–40], where passivation occurs.

We performed top-view scanning electron microscopy (SEM) measurements on the MAPbI₃ films with various PEA concentrations (Fig. 2a–d). The control MAPbI₃ film presents a compact surface morphology, with grain sizes ranging from 100 to 300 nm. After 0.1 wt% PEA is added, the grain size decreases slightly. The size decrease is due to the inability of PEA, to freely migrate, which has long molecule chain to hinder the growth of the perovskite

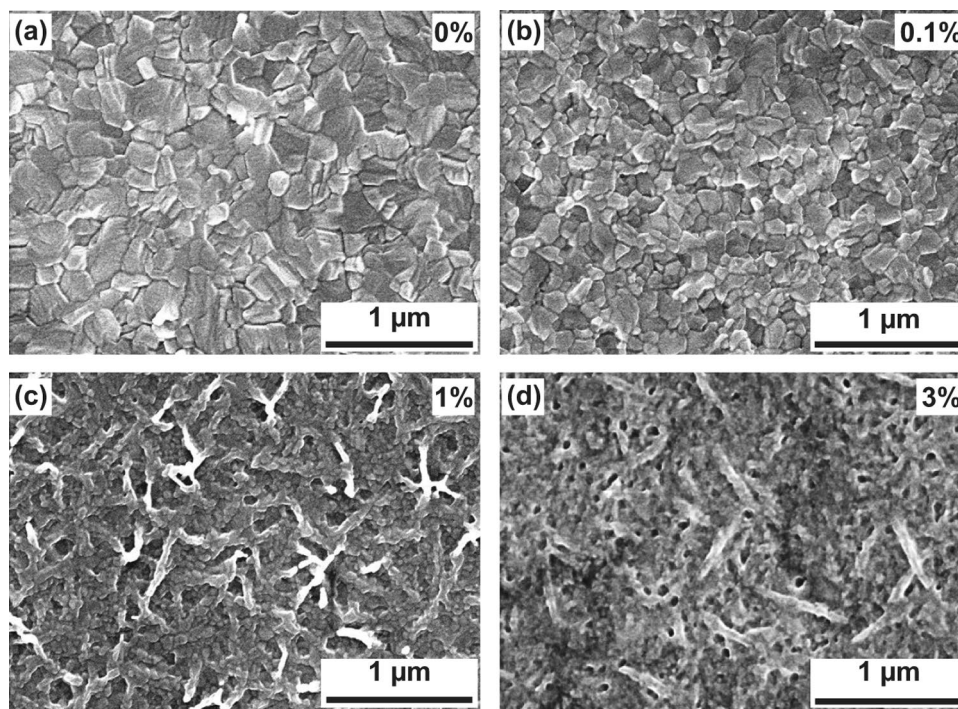


Fig. 2 Top view SEM images of the MAPbI₃ films with different PEA concentrations with **a** 0 wt%, **b** 0.1 wt%, **c** 1 wt%, and **d** 3 wt%

crystal [40]. As the PEA concentration is increased to 1 wt%, branchlike features began to appear around GBs and on the surface, implying that the PEA molecules start to bridge the perovskite grains and occupy the perovskite surface. These branchlike features increase with increasing PEA concentration. When the PEA concentration is up to 3 wt%, most of the surface is covered by the branchlike features. Owing to the weak conductive ability of PEA, it is expected that a thick PEA layer coating on the perovskite film would weaken the electron tunneling and hinders charge transfer. In addition, we performed cross-section SEM on the MAPbI₃ films with (1 wt%) and without PEA (Fig. S4). The control film exhibits a bumpy surface, while the MAPbI₃ film with PEA displays a smooth surface.

X-ray diffraction (XRD) tests for the MAPbI₃ films with and without PEA were conducted. Figure 3a indicates that the main diffraction peaks of the two films locate at the same positions of approximately 14.1°, 28.4°, and 31.9°, which are consistent with the diffraction peaks of (110), (220), and (310) planes of the perovskite crystal, respectively [41]. Compared to the control film, the diffraction peak intensity of the MAPbI₃ film with PEA increases slightly, indicating an enhanced crystallinity. From the

XRD spectra, we can conclude that the PEA additive is beneficial for the perovskite crystallization without affecting the perovskite crystal chemical structure. The absorption spectra of the MAPbI₃ films with and without PEA are provided in Fig. 3b. The two films present same absorption edges, demonstrating that the band gap of the perovskite remains unchanged. The MAPbI₃ film with PEA presents a slightly higher absorbance than the control film in the range from 400 to 750 nm, indicating a better crystallinity [42]. The thermal and light stabilities of the two films are compared (Fig. 3c, d). The control MAPbI₃ film is unable to endure both the thermal test (80 °C for 70 h) and the light test (white light LED of 1 sun light intensity for 300 h), while the film with PEA remains undamaged. After the tests, a new XRD peak at 12.7°, which corresponds to the (001) diffraction peak of PbI₂ [43], appears for the control film, but not for the MAPbI₃ film with PEA. The reasons for the retarded film degradation in the presence of PEA passivation could be explained as follows: Firstly, PEA could enhance perovskite crystallization. Secondly, PEA-perovskite interaction can suppress thermally induced and light-induced ions movement and desorption from the crystal [39, 44, 45].

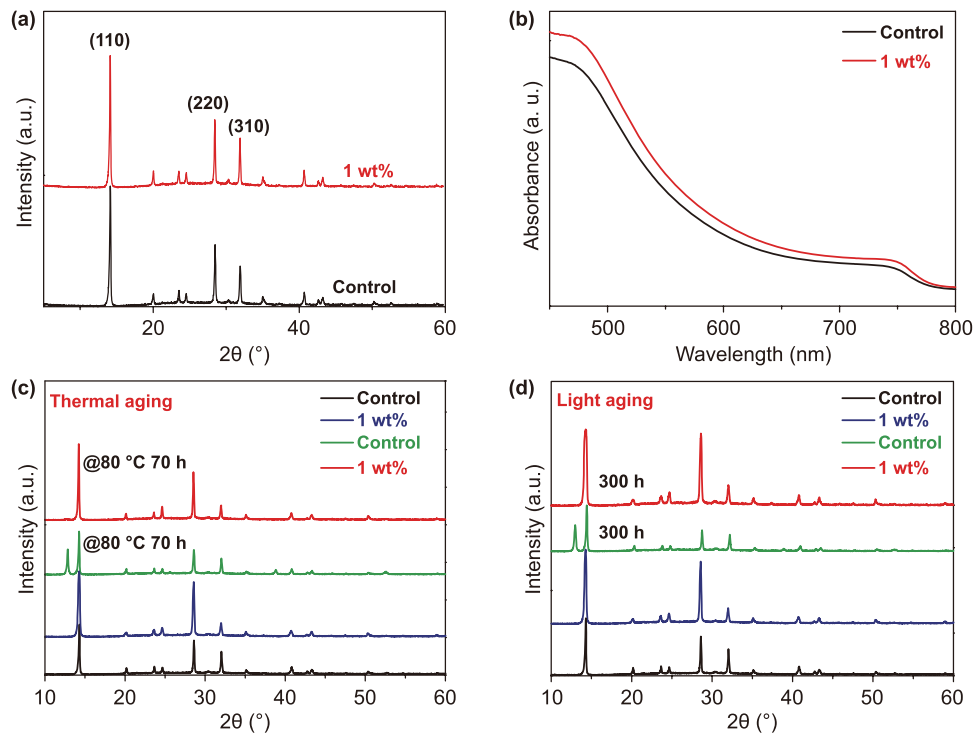


Fig. 3 **a** XRD spectra, **b** UV–Vis absorption spectra of the MAPbI₃ films with and without PEA. **c** XRD spectra of the MAPbI₃ films with and without PEA, before and after thermal aging at 80 °C for 70 h, and **d** light aging for 300 h

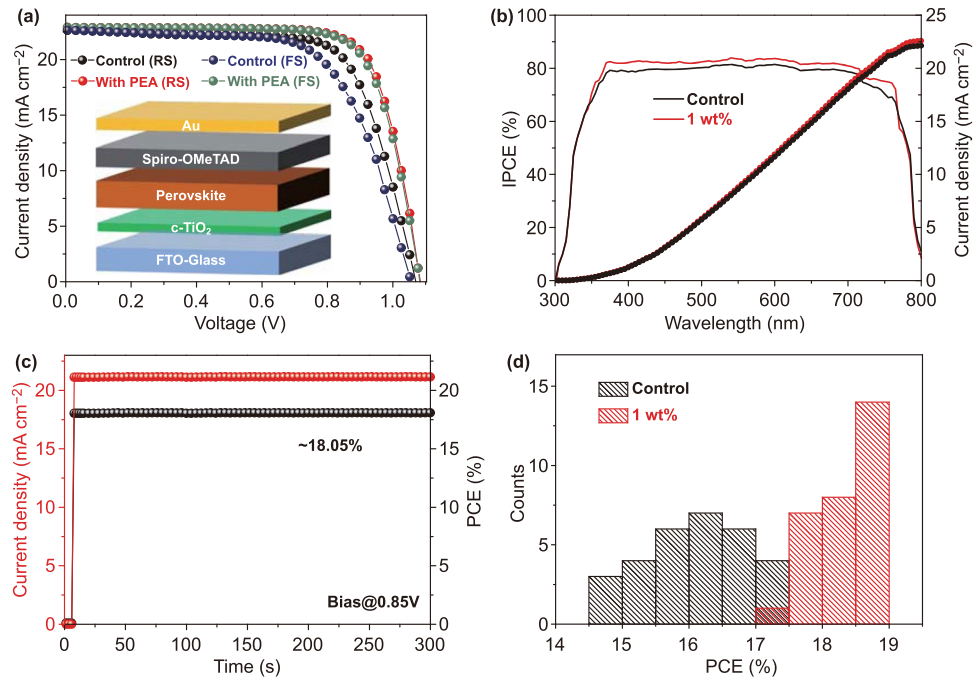


Fig. 4 **a** *J*–*V* curves of the MAPbI₃ devices with and without PEA (the inset gives the device structure). **b** IPCE spectra and integrated *J*_{SC} of the two devices. **c** Steady-state current density and PCE at a constant bias of 0.85 V for the device with PEA. **d** Histogram of PCE distribution

Planar heterojunction structure (PHJ) solar cells with a configuration of FTO-coated glass/TiO₂/MAPbI₃/Spiro-OMeTAD/Au were fabricated. By optimization, the concentration of 1 wt% PEA leads to the optimal performance of PSCs (Fig. S5 and Table S1). Figure 4a shows the best PCE from the device with 1 wt% PEA. The detailed device parameters are provided in Table S2. Under reverse scan, the MAPbI₃ device with PEA exhibits a PCE of 18.87%, with V_{OC} of 1.08 V, J_{SC} of 22.89 mA cm⁻², and FF of 76.3%. It outperforms the control device, which exhibits a PCE of 17.18%, with V_{OC} of 1.08 V, J_{SC} of 22.63 mA cm⁻², and FF of 70.3%. The improved PCE is mainly ascribed to the improvement of J_{SC} and FF, which benefited from enhanced charge transport. In addition, hysteresis index (HI) values are calculated by Eq. (1) [20]:

$$HI = \frac{PCE_{reverse} - PCE_{forward}}{PCE_{reverse}} \quad (1)$$

The device with PEA has a HI value of 0.011, which is significantly less than that of the control device (0.091). The negligible hysteresis can be attributed to efficient defect passivation by PEA. The incident photon to current conversion efficiency (IPCE) and integrated J_{SC} of the two devices are

shown in Fig. 4b. Compared to the control device, the device with PEA has a higher spectral response in the range of 400–750 nm. The calculated integrated J_{SC} from the IPCE spectrum of the device with PEA is 22.58 mA cm⁻², and that of the control device is 22.11 mA cm⁻². Both these results concurred with those from J - V curves. We also recorded the photocurrent density and the PCE of the device with PEA and the control device as a function of time biased at its maximum power point voltage for 300 s. As shown in Figs. S6 and Fig. 4c, the PCEs quickly stabilize at 18.05% and 16.22%, respectively. To evaluate the reproducibility of the devices, two batches of 30 cells are fabricated. The histogram in Fig. 4d shows that the devices with PEA exhibit enhanced PCEs with narrower distributions.

Figure 5a presents the steady-state photoluminescence (PL) spectra of the MAPbI₃ films with and without PEA on glass substrates. It is apparent that the PL peaks of the two films locate at the same energy position, and the MAPbI₃ film with PEA shows stronger PL intensity. This demonstrates that nonradiative recombination in the perovskite film is suppressed. To explore the impact of PEA on charge carrier dynamics, time-resolved PL (TRPL) decay measurements of the two films were conducted, and

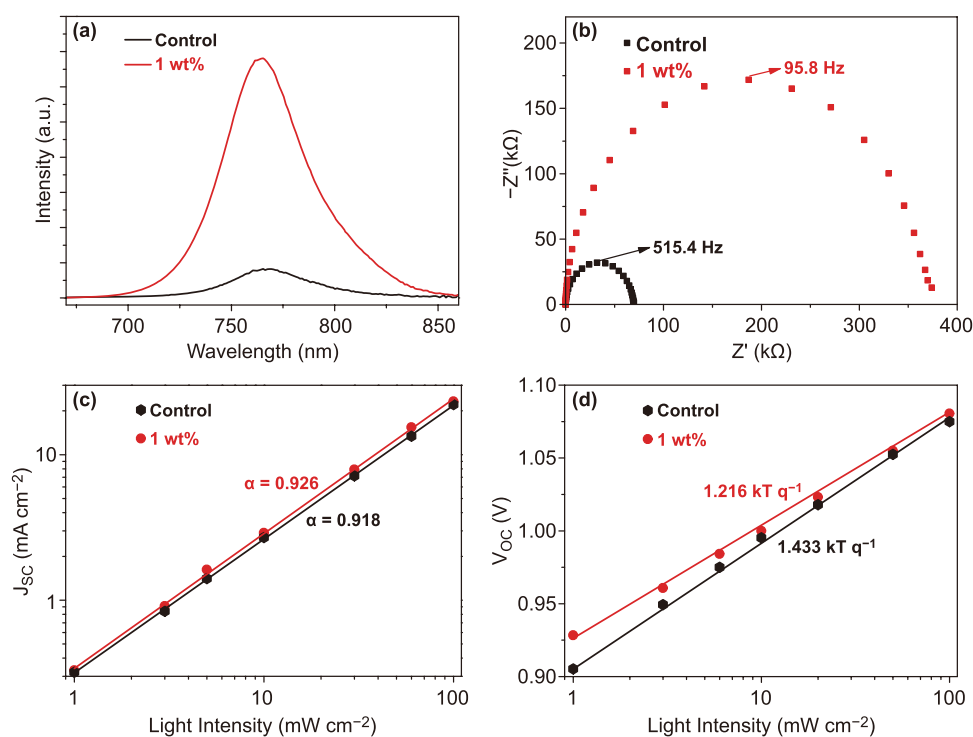


Fig. 5 a PL of the MAPbI₃ films with and without PEA on glass substrates. b EIS spectra, c J_{SC} versus light intensity, and d V_{OC} versus light intensity of MAPbI₃ devices with and without PEA

the spectra are displayed in Fig. S7. The PL kinetics are fitted by the biexponential function below [Eq. (2)] [46]:

$$Y = A_1 \exp\left(-\frac{t}{\tau_1}\right) + A_2 \exp\left(-\frac{t}{\tau_2}\right) + y_0 \quad (2)$$

where τ_1 and τ_2 are the lifetimes of the fast and slow recombination processes [47], and A_1 and A_2 represent the corresponding relative amplitudes. Detailed fitting parameters are summarized in Table S3. After PEA is added, τ_1 and τ_2 are prolonged from 4.2 and 42.5 ns to 6.0 and 69.3 ns, respectively. Furthermore, the PL lifetimes were also measured when the two films are interfaced with PCBM and Spiro-OMeTAD (Fig. S8). τ_1 and τ_2 are 2.8 and 6.8 ns for the PEA modified MAPbI₃ film/PCBM, and are 3.9 and 9.4 ns for the MAPbI₃ film/PCBM. The lifetimes are also shortened for the PEA modified MAPbI₃ film/Spiro-OMeTAD, with τ_1 and τ_2 of 6.2 and 22.2 ns, as compared to 5.3 and 33.1 ns for the MAPbI₃ film/Spiro-OMeTAD (Table S4). These results indicate suppressed charge recombination and enhanced charge transfer in the MAPbI₃ film with PEA [48]. Electrical impedance spectroscopy (EIS) was performed on the MAPbI₃ devices with and without PEA under open-circuit conditions in a dark environment (Fig. 5b). It is apparent that the device with PEA has larger recombination resistance R_{rec} , indicating that the film with PEA is in favor of suppressing carrier recombination [49, 50]. In addition, the carrier lifetimes are also estimated from EIS from Eq. (3) [51–53]:

$$\tau = \frac{1}{2\pi f} \quad (3)$$

where f is the frequency of the highest point in EIS. The calculated τ is 0.31 ms for the control device, and 1.66 ms for the device with PEA. This longer carrier lifetime further demonstrates the PEA passivation benefit.

To estimate carrier trap state density in the MAPbI₃ films with and without PEA, we performed space-charge-limited current (SCLC) measurements on hole-only and electron-only devices (Fig. S9, Supporting Information). The trap state densities are calculated from Eq. (4) [54]:

$$N_t = \frac{2V_{\text{TFL}}\epsilon_0\epsilon_r}{qL^2} \quad (4)$$

where V_{TFL} is the onset voltage of the trap-filled limit region in the dark J - V curves, ϵ_0 and ϵ_r represent the vacuum permittivity and the relative dielectric constant of MAPbI₃, respectively, and L is the thickness of the perovskite film. The result shows that the hole (electron) trap state density is decreased from 7.2×10^{15} to 4.5×10^{15} cm⁻³ (9.5×10^{15} to 5.5×10^{15} cm⁻³).

We then explored the variation of J_{SC} and V_{OC} under different light intensities. The power law dependence of J_{SC} on the incident light intensity P_{light} for the investigated devices is displayed in Fig. 5c, and the data are fitted by Eq. (5) [55–57]:

$$J_{\text{SC}} \propto P_{\text{light}}^\alpha \quad (5)$$

Without recombination, α value is 1. In practice, α will be lower than 1 because there always exists carrier recombination in a solar cell device [58–60]. The larger α is, the weaker the recombination is. The device with PEA has a larger α than the control device (0.926 vs 0.918), confirming that carrier recombination is suppressed in the device with PEA. We also investigated the dependence of V_{OC} on P_{light} and found V_{OC} is logarithmically dependent on P_{light} (Fig. 5d). The diode ideality factor n can be expressed by Eq. (6) [50, 61]:

$$n \approx \frac{q}{kT} \frac{dV_{\text{OC}}}{d \lg(P_{\text{light}})} \quad (6)$$

where k , q , T are Boltzmann constant, elementary charge and temperature, respectively. For an ideal device, n equals 1. For a non-ideal device, n is larger than 1, and the larger n , the stronger the carrier recombination [62, 63]. The control device possesses a large n value of 1.433, suggesting severe carrier recombination inside the device. In contrast, the device with PEA exhibits a smaller n value of 1.216, indicating that carrier recombination is suppressed by PEA.

We then investigated the stability of the two devices in air stored in a dark environment. Figure 6a–d displays V_{OC} , J_{SC} , FF, and PCE variation in air (with $30 \pm 5\%$ relative humidity). The MAPbI₃ device with PEA remains at 95% of its original PCE after 30 days, while the control device only retains 60% of its original value. This significant improvement in stability could be primarily attributed to PEA filling the GB gaps, which plays a crucial role in blocking H₂O and O₂. Furthermore, PEA is hydrophobic and hence would naturally repel H₂O. The perovskite film became less hydrophilic when PEA is added (Fig. S10a, b). The MAPbI₃ film with PEA shows a contact angle of 63.3°, while the control film shows a contact angle of 37.2°.

2.2 Characterization of (FAPbI₃)_{1-x}(MAPbBr₃)_x Devices with PEA

Finally, we applied PEA to (FAPbI₃)_{1-x}(MAPbBr₃)_x (details are described in the Experimental Section). Figure 7a

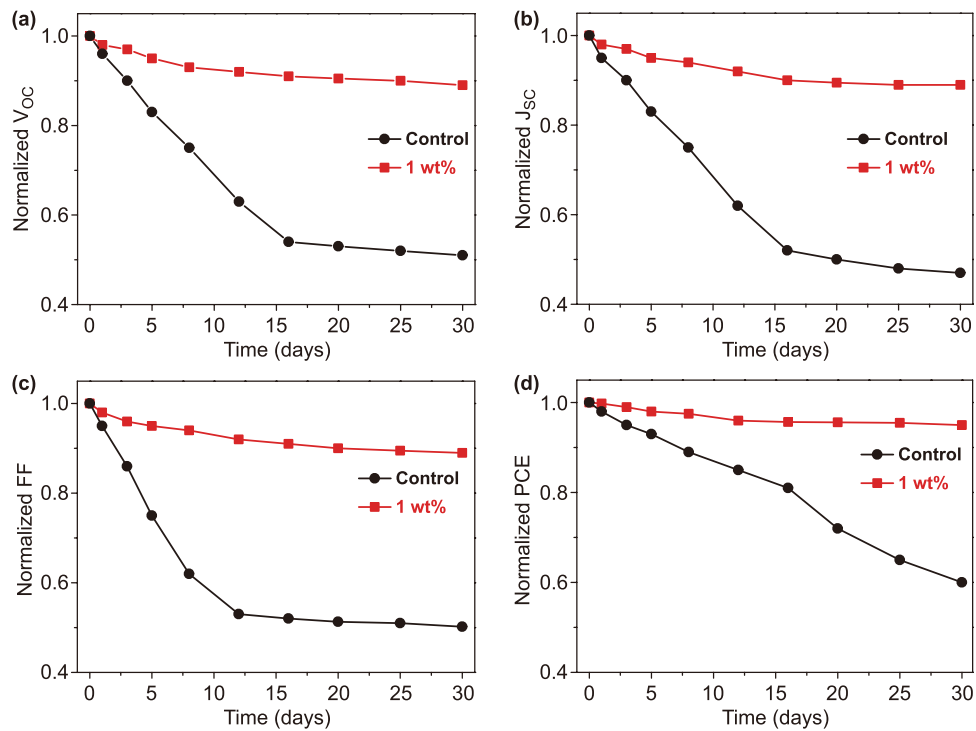


Fig. 6 Normalized **a** V_{OC} , **b** J_{SC} , **c** FF, and **d** PCE of the MAPbI₃ devices with and without PEA vs time. The devices are stored in a dark environment under ambient air with $30 \pm 5\%$ relative humidity

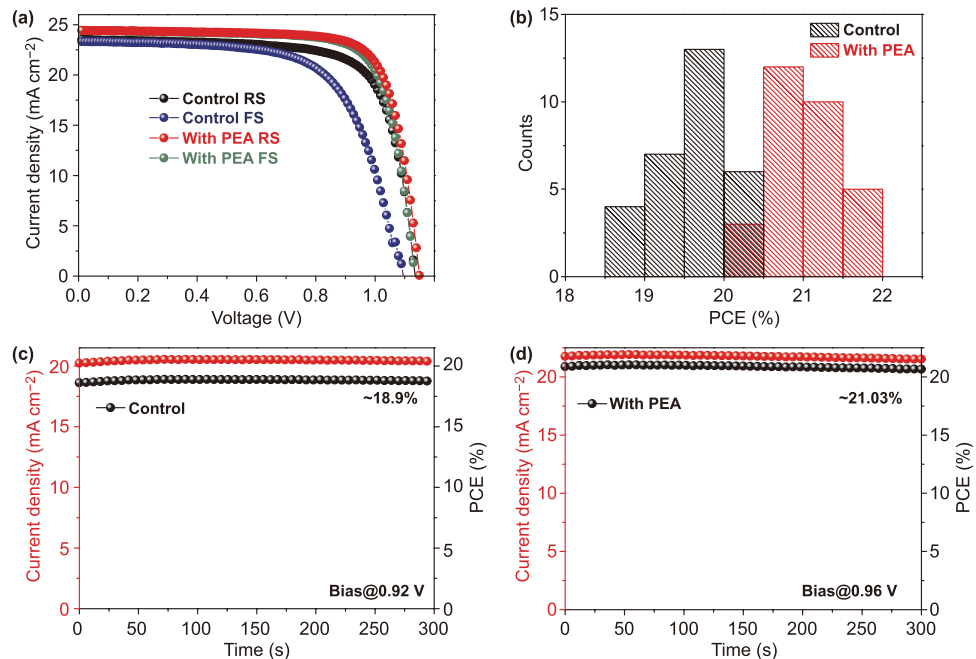


Fig. 7 **a** $J-V$ curves of the (FAPbI₃)_{1-x}(MAPbBr₃)_x PSCs with and without PEA. **b** Histogram of PCE distribution. **c** Steady-state current density and efficiency at maximum power point of the device without, and **d** with PEA

demonstrates J - V characteristics of the corresponding devices with and without PEA. The device parameters are displayed in Table S5. The control device exhibits a PCE of 19.66%, with V_{OC} of 1.13 V, J_{SC} of 23.51 mA cm⁻², and FF 73.7%, while the device with PEA delivers a significantly improved PCE of 21.60%, with V_{OC} of 1.15 V, J_{SC} of 24.42 mA cm⁻², and FF of 76.9%. In addition, the control device shows a very high HI of 0.15, while the device with PEA is significantly lower, at 0.02. Their PCEs distributions are provided in Fig. 7b. Figure 7c, d shows the steady-state efficiency at maximum power point for the control device and the device with PEA, respectively. It is observed the PCE of the device with PEA stabilizes at 21.02%, while that of the control device remains at 18.90%.

3 Conclusion

We employed PEA for perovskite surface and GB passivation. The ether-oxygen unshared electron pair in PEA activates to form a crosslinking complex with lead ions, resulting in the decrease in trap state density and inhibition of non-radiative recombination in the perovskite films. The MAPbI₃-based cells with PEA obtain an improved PCE from 17.18 to 18.87%, with significantly reduced hysteresis from 9.1 to 1.1%. Moreover, the device maintains 95% of its original PCE after 30 days without any encapsulation. In contrast, the control device retains only 60% of its initial PCE under the same condition. For (FAPbI₃)_{1-x}(MAPbBr₃)_x-based cells, the hysteresis is significantly suppressed from 15.0 to 2.0%, and the PCE is enhanced from 19.66 to 21.60%. This work demonstrates that PEA is a very efficient trap passivator for stable high-efficiency PSCs.

4 Experimental Section

4.1 Materials

PbI₂, MAI, FAI, MABr, Spiro-OMeTAD, and Li-TFSI are purchased from Xi'an Baolaite Technology Crop. TiCl₄, SnO₂ colloid precursor (15% in H₂O colloidal dispersion), PEA, DMF, DMSO and chlorobenzene are purchased from Alfa Aesar. 4-tert-butylpyridine (TBP, 96% purity), PCBM, PEDOT: PSS are obtained from Sigma-Aldrich. All of the above materials and chemicals are used as received.

4.2 Solution Preparation

The MAPbI₃ precursor solution (199 mg MAI and 461 mg PbI₂ dissolved in 800 μL DMF and 200 μL DMSO mixed solvent) is prepared in a N₂ glove box. The PEA additive (concentration varying from 0 wt% to 3 wt%) is added in the MAPbI₃ precursor solution and is further stirred for 2 h at 60 °C on a hotplate. The solution is filtered before use. The (FAPbI₃)_{1-x}(MAPbBr₃)_x film is prepared by a two-step spin-coating process. PbI₂ solution (760 mg PbI₂ in 1000 μL DMF and 160 μL DMSO) is added by 0.1 wt% PEA additive and is stirred for 2 h at 60 °C. The mixed organic salt solution for the second step is 73.3 mg FAI/7.7 mg MACl/7.3 mg MABr in 1 mL IPA solvent. The Spiro-OMeTAD solution is obtained by dissolving 72.3 mg Spiro-OMeTAD, 35 μL Li-TFSI solution (260 mg mL⁻¹ in acetonitrile), and 28.8 μL TBP in 1 mL of chlorobenzene.

4.3 Fabrication of PSCs

MAPbI₃ devices FTO-coated glass is sequentially ultrasonically cleaned in deionized water, acetone, and isopropanol. The substrate is then dried by N₂ flow and treated by ozone plasma for 15 min. Prior to depositing the perovskite layer, the TiO₂ electron transport layer is fabricated by immersing the substrate in hot (70 °C) TiCl₄ aqueous solution (with a concentration of 200 mM) for 1 h, and is further heated at 100 °C for 1 h. The MAPbI₃ precursor is spin-coated by a successive procedure of 1000 rpm for 10 s and 4000 rpm for 30 s on top of the TiO₂ film. In the second step, 20 s before the ending of the procedure, 100 μL chlorobenzene is rapidly dropped onto the surface of the sample. Afterwards, the sample is annealed at 100 °C for 10 min and subsequently, the Spiro-OMeTAD solution is spin-coated on the perovskite film at 4000 rpm for 30 s. The sample is then preserved in a dry dark box for 20 h. The device is completed by thermally deposition a 70-nm Au electrode.

(FAPbI₃)_{1-x}(MAPbBr₃)_x devices ITO-coated glass is sequentially ultrasonically cleaned in deionized water, acetone, isopropanol, dried by N₂ flow, and then treated by ozone plasma for 15 min. The SnO₂ electron transport layer is deposited on the ITO substrate by spin-coating

the SnO₂ precursor (2%, diluted by water) at 3000 rpm for 30 s, and then heated at 150 °C for 30 min. The (FAPbI₃)_{1-x}(MAPbBr₃)_x film is fabricated by spin-coating the PbI₂ solution at 1600 rpm for 10 s and then 4000 rpm for 30 s. The film is annealed at 70 °C for 2 min, followed by spin-coating the mixed solution (FAI/MACI/MABr) at 2000 rpm for 23 s and an annealing process at 140 °C for 20 min in air. The following steps for Spiro-OMeTAD film and Au electrode replicate those for the MAPbI₃ devices.

Hole-only devices The PEDOT: PSS is prepared by spin-coating the solution at 2000 rpm for 50 s on the ITO substrates, and is heated at 140 °C for 10 min. The perovskite film is then deposited using the previous method. The Spiro-OMeTAD layer is then fabricated by spin-coating at 2000 rpm for 50 s. Finally, a 70-nm Au electrode underwent thermal deposition.

Electron-only devices The SnO₂ layer and the perovskite layer are sequentially deposited on the ITO substrates using the previous method. The PCBM layer is then made from a precursor solution (15 mg mL⁻¹ in chlorobenzene) via spin-coating at 2000 rpm for 50 s. Finally, a 100 nm Ag electrode underwent thermal deposition.

4.4 Characterization

TOF-SIMS tests in the positive ion mode were conducted on a ToF-SIMS V instrument (ION-TOF GmbH, Münster, Germany). A pulsed 30 keV Bi₃⁺ primary ion beam was used for the analysis with the beam current of 0.98 pA at a pulse repeating frequency of 10 kHz. The sputtering beam was 10 keV Ar₁₇₀₀⁺ with the beam current adjusted to 2 nA. The analysis area was 100 × 100 μm² at the center of a crater of 250 × 250 μm². During the measurements, a low-energy flood gun was used for charge compensation. FTIR spectra were tested by TENSOR-27 (Bruker, Germany), and the XPS result was obtained by ESCALAB250XI (VG, America). SEM images were obtained by S-4800 (Hitachi, Japan). XRD is performed on D/max 2500 (Rigaku, Japan) with a Cu Kα radiation source (λ = 1.5418 Å). UV-Vis absorption spectra were characterized by UV-2600 (SHIMADZ, Japan). *J*–*V* curves were obtained by a Keithley 2400 system, with a light intensity of 100 mW cm⁻² under an AM 1.5 solar simulator. IPCE spectra were recorded by a computer-controlled system. PL and TRPL spectra were recorded by a spectrofluorometer (FLS980, Edinburgh, England). EIS

was performed on an IM6ex Electrochemical Workstation (Zahener, Germany), and the frequency range used is 1 MHz to 1 Hz.

Acknowledgements Financial support for this research is provided by the National Key Research Program of China (2016YFA0200104) and the Strategic Priority Research Program of the Chinese Academy of Sciences (XDB12030200).

Open Access This article is licensed under a Creative Commons Attribution 4.0 International License, which permits use, sharing, adaptation, distribution and reproduction in any medium or format, as long as you give appropriate credit to the original author(s) and the source, provide a link to the Creative Commons licence, and indicate if changes were made. The images or other third party material in this article are included in the article's Creative Commons licence, unless indicated otherwise in a credit line to the material. If material is not included in the article's Creative Commons licence and your intended use is not permitted by statutory regulation or exceeds the permitted use, you will need to obtain permission directly from the copyright holder. To view a copy of this licence, visit <http://creativecommons.org/licenses/by/4.0/>.

Electronic supplementary material The online version of this article (<https://doi.org/10.1007/s40820-020-00517-y>) contains supplementary material, which is available to authorized users.

References

1. M.M. Lee, J. Teuscher, T. Miyasaka, T.N. Murakami, H.J. Snaith, Efficient hybrid solar cells based on meso-structured organometal halide perovskites. *Science* **338**(6107), 643–647 (2012). <https://doi.org/10.1126/science.1228604>
2. S.D. Stranks, G.E. Eperon, G. Grancini, C. Menelaou, M.J.P. Alcocer et al., Electron-hole diffusion lengths exceeding 1 micrometer in an organometal trihalide perovskite absorber. *Science* **342**(6156), 341–344 (2013). <https://doi.org/10.1126/science.1243982>
3. C. Wehrenfennig, G.E. Eperon, M.B. Johnston, H.J. Snaith, L.M. Herz, High charge carrier mobilities and lifetimes in organolead trihalide perovskites. *Adv. Mater.* **26**(10), 1584–1589 (2014). <https://doi.org/10.1002/adma.201305172>
4. H. Zhou, Q. Chen, G. Li, S. Luo, T.B. Song et al., Interface engineering of highly efficient perovskite solar cells. *Science* **345**(6196), 542–546 (2014). <https://doi.org/10.1126/science.1254050>
5. N.J. Jeon, J.H. Noh, W.S. Yang, Y.C. Kim, S. Ryu, J. Seo, S.I. Seok, Compositional engineering of perovskite materials for high-performance solar cells. *Nature* **517**, 476–480 (2015). <https://doi.org/10.1038/nature14133>
6. A. Kojima, K. Teshima, Y. Shirai, T. Miyasaka, Organometal halide perovskites as visible-light sensitizers for photovoltaic cells. *J. Am. Chem. Soc.* **131**(17), 6050–6051 (2009). <https://doi.org/10.1021/ja809598r>

7. National renewable energy laboratory, Best research-cell efficiencies. www.nrel.gov/pv/assets/pdfs/best-research-cell-efciencies.20190802.pdf
8. T. Matsui, H. Jia, M. Kondo, Thin film solar cells incorporating microcrystalline $\text{Si}_{1-x}\text{Ge}_x$ as efficient infrared absorber: an application to double junction tandem solar cells. *Prog. Photovoltaics Res. Appl.* **18**(1), 48–53 (2010). <https://doi.org/10.1002/pip.922>
9. W. Ke, C. Xiao, C. Wang, B. Saparov, H.S. Duan et al., Employing lead thiocyanate additive to reduce the hysteresis and boost the fill Factor of planar perovskite solar cells. *Adv. Mater.* **28**(26), 5214–5221 (2016). <https://doi.org/10.1002/adma.201600594>
10. Y. Zhang, L. Tan, Q. Fu, L. Chen, T. Ji, X. Hu, Y. Chen, Enhancing the grain size of organic halide perovskites by sulfonate-carbon nanotube incorporation in high performance perovskite solar cells. *Chem. Commun* **52**, 5674 (2016). <https://doi.org/10.1039/c6cc00268d>
11. Q. Chen, H. Zhou, T. Bin Song, S. Luo, Z. Hong et al., Controllable self-induced passivation of hybrid lead iodide perovskites toward high performance solar cells. *Nano Lett.* **14**(7), 4158–4163 (2014). <https://doi.org/10.1021/ml501838y>
12. M. Saliba, T. Matsui, K. Domanski, J.Y. Seo, A. Ummadisingu et al., Incorporation of rubidium cations into perovskite solar cells improves photovoltaic performance. *Science* **354**(6309), 206–209 (2016). <https://doi.org/10.1126/science.aah5557>
13. M. Kot, C. Das, Z. Wang, K. Henkel, Z. Rouissi et al., Room-temperature atomic layer deposition of Al_2O_3 : impact on efficiency, stability and surface properties in perovskite solar cells. *Chemsuschem* **9**(24), 3401–3406 (2016). <https://doi.org/10.1002/cssc.201601186>
14. L. Chu, W. Ahmad, W. Liu, J. Yang, R. Zhang et al., Lead-free halide double perovskite materials: a new superstar towards green and stable optoelectronic applications. *Nano-Micro Lett.* **11**, 16 (2019). <https://doi.org/10.1007/s40820-019-0244-6>
15. F. Wang, W. Geng, Y. Zhou, H.-H. Fang, C.-J. Tong et al., Perovskites enabling high-efficiency and air-stable photovoltaic cells. *Adv. Mater.* **28**, 9986–9992 (2016). <https://doi.org/10.1002/adma.201603062>
16. F. Wang, A. Shimazaki, F. Yang, K. Kanahashi, K. Matsuki et al., Highly efficient and stable perovskite solar cells by interfacial engineering using solution-processed polymer layer. *J. Phys. Chem. C* **121**, 1562–1568 (2017). <https://doi.org/10.1021/acs.jpcc.6b12137>
17. W. Liu, N. Liu, S. Ji, H. Hua, Y. Ma et al., Perfection of perovskite grain boundary passivation by rhodium incorporation for efficient and stable solar cells. *Nano-Micro Lett.* **12**, 119 (2020). <https://doi.org/10.1007/s40820-020-00457-7>
18. M.E. Kayesh, T.H. Chowdhury, K. Matsuiishi, R. Kaneko, S. Kazaoui et al., Enhanced photovoltaic performance of FASnI_3 -based perovskite solar cells with hydrazinium chloride coadditive. *ACS Energy Lett.* **3**(7), 1584–1589 (2018). <https://doi.org/10.1021/acsenerylett.8b00645>
19. L. Liu, S. Huang, Y. Lu, P. Liu, Y. Zhao et al., Grain-boundary “patches” by in situ conversion to enhance perovskite solar cells stability. *Adv. Mater.* **30**(29), 1800544 (2018). <https://doi.org/10.1002/adma.201800544>
20. J. Jiang, Q. Wang, Z. Jin, X. Zhang, J. Lei et al., Polymer doping for high-efficiency perovskite solar cells with improved moisture stability. *Adv. Energy Mater.* **8**(3), 1701757 (2018). <https://doi.org/10.1002/aenm.201701757>
21. L. Meng, C. Sun, R. Wang, W. Huang, Z. Zhao et al., Tailored phase conversion under conjugated polymer enables thermally stable perovskite solar cells with efficiency exceeding 21%. *J. Am. Chem. Soc.* **140**(49), 17255–17262 (2018). <https://doi.org/10.1021/jacs.8b10520>
22. J. Wei, H. Li, Y. Zhao, W. Zhou, R. Fu et al., Suppressed hysteresis and improved stability in perovskite solar cells with conductive organic network. *Nano Energy* **26**, 139–147 (2016). <https://doi.org/10.1016/j.nanoen.2016.05.023>
23. L. Zuo, H. Guo, D.W. deQuilettes, S. Jariwala, N. De Marco et al., Polymer-modified halide perovskite films for efficient and stable planar heterojunction solar cells. *Sci. Adv.* **3**, e1700106 (2017). <https://doi.org/10.1126/sciadv.1700106>
24. P.-L. Qin, G. Yang, Z.-W. Ren, S.H. Cheung, S.K. So et al., Stable and efficient organo-metal halide hybrid perovskite solar cells via π -conjugated Lewis base polymer induced trap passivation and charge extraction. *Adv. Mater.* **30**(12), 1706126 (2018). <https://doi.org/10.1002/adma.201706126>
25. A. Ng, Z. Ren, Q. Shen, S.H. Cheung, H.C. Gokkaya et al., Crystal engineering for low defect density and high efficiency hybrid chemical vapor deposition grown perovskite solar cells. *ACS Appl. Mater. Interfaces* **8**(48), 32805–32814 (2016). <https://doi.org/10.1021/acsami.6b07513>
26. W.-J. Yin, H. Chen, T. Shi, S.-H. Wei, Y. Yan, Origin of high electronic quality in structurally disordered $\text{CH}_3\text{NH}_3\text{PbI}_3$ and the passivation effect of Cl and O at grain boundaries. *Adv. Electron. Mater.* **1**(6), 1500044 (2015). <https://doi.org/10.1002/aelm.201500044>
27. P. Qin, T. Wu, Z. Wang, X. Zheng, X. Yu, G. Fang, G. Li, Vitrification transformation of poly(ethylene oxide) activating interface passivation for high-efficiency perovskite solar cells. *Sol. RRL* **3**, 1900134 (2019). <https://doi.org/10.1002/solr.201900134>
28. M. Kim, S.G. Motti, R. Sorrentino, A. Petrozza, Enhanced solar cell stability by hygroscopic polymer passivation of metal halide perovskite thin film. *Energy Environ. Sci.* **11**, 2609–2619 (2018). <https://doi.org/10.1039/C8EE01101J>
29. P. Guo, Q. Ye, X. Yang, J. Zhang, F. Xu et al., Surface & grain boundary co-passivation by fluorocarbon based bifunctional molecules for perovskite solar cells with efficiency over 21%. *J. Mater. Chem. A* **7**, 2497–2506 (2019). <https://doi.org/10.1039/c8ta11524a>
30. P. Qin, Q. He, G. Yang, X. Yu, L. Xiong, G. Fang, Metal ions diffusion at heterojunction chromium Oxide/ $\text{CH}_3\text{NH}_3\text{PbI}_3$ interface on the stability of perovskite solar cells. *Surf. Interfaces* **10**, 93–99 (2018). <https://doi.org/10.1016/j.surfin.2017.12.006>
31. R. Morent, N. De Geyter, C. Leys, L. Gengembreb, Comparison between XPS- and FTIR- analysis of plasma-treated



- polypropylene film surfaces. *E. Payenb. Surf. Interface Anal.* **40**, 597–600 (2008). <https://doi.org/10.1002/sia.2619>
32. W. Zhou, D. Li, Z. Xiao, Z. Wen, M. Zhang et al., Zwitterion coordination induced highly orientational order of $\text{CH}_3\text{NH}_3\text{PbI}_3$ perovskite film delivers a high open circuit voltage exceeding 1.2 V. *Adv. Funct. Mater.* **29**(23), 1901026 (2019). <https://doi.org/10.1002/adfm.201901026>
 33. S. Yang, S. Chen, E. Mosconi, Y. Fang, X. Xiao et al., Stabilizing halide perovskite surfaces for solar cell operation with wide-bandgap lead oxysalts. *Science* **365**(6452), 473–478 (2019). <https://doi.org/10.1126/science.aax3294>
 34. J.-W. Lee, D.-H. Kim, H.-S. Kim, S.-W. Seo, S.M. Cho, N.-G. Park, Formamidinium and cesium hybridization for photo- and moisture- stable perovskite solar cell. *Adv. Energy Mater.* **5**(20), 1501310 (2015). <https://doi.org/10.1002/aenm.201501310>
 35. B. Li, J. Zhen, Y. Wan, X. Lei, Q. Liu et al., Anchoring fullerene onto perovskite film via grafting pyridine toward enhanced electron transport in high-efficiency solar cells. *ACS Appl. Mater. Interfaces* **10**(38), 32471–32482 (2018). <https://doi.org/10.1021/acsami.8b11459>
 36. R. Lindblad, D. Bi, B.W. Park, J. Oscarsson, M. Gorgoi et al., Electronic structure of $\text{TiO}_2/\text{CH}_3\text{NH}_3\text{PbI}_3$ perovskite solar cell interfaces. *J. Phys. Chem. Lett.* **5**(4), 648–653 (2014). <https://doi.org/10.1021/jz402749f>
 37. D. Bi, C. Yi, J. Luo, J.D. Décoppet, F. Zhang et al., Polymer-templated nucleation and crystal growth of perovskite films for solar cells with efficiency greater than 21%. *Nat. Energy* **1**, 16142 (2016). <https://doi.org/10.1038/nenergy.2016.142>
 38. Y. Wu, X. Yang, W. Chen, Y. Yue, M. Cai et al., Perovskite solar cells with 18.21% efficiency and area over 1 cm^2 fabricated by heterojunction engineering. *Nat. Energy* **1**, 16148 (2016). <https://doi.org/10.1038/nenergy.2016.148>
 39. T. Niu, J. Liu, R. Munir, J. Li, D. Barrit et al., Stable high-performance perovskite solar cells via grain boundary passivation. *Adv. Mater.* **30**(16), 1706576 (2018). <https://doi.org/10.1002/adma.201706576>
 40. W. Chen, Y. Wang, G. Pang, C.W. Koh, A.B. Djurišić et al., Conjugated polymer-assisted grain boundary passivation for efficient inverted planar perovskite solar cells. *Adv. Funct. Mater.* **29**(27), 1808855 (2019). <https://doi.org/10.1002/adfm.201808855>
 41. C. Sun, Y. Guo, B. Fang, J. Yang, B. Qin et al., Enhanced photovoltaic performance of perovskite solar cells using polymer P(VDF-TrFE) as a processed additive. *J. Phys. Chem. C* **120**(24), 12980–12988 (2016). <https://doi.org/10.1021/acs.jpcc.6b05255>
 42. H. Cho, S.H. Jeong, M.H. Park, Y.H. Kim, C. Wolf et al., Overcoming the electroluminescence efficiency limitations of perovskite light-emitting diodes. *Science* **350**(6265), 1222–1225 (2015). <https://doi.org/10.1126/science.aad1818>
 43. X. Dong, X. Fang, M. Lv, B. Lin, S. Zhang, J. Ding, N. Yuan, Improvement of the humidity stability of organic–inorganic perovskite solar cells using ultrathin Al_2O_3 layers prepared by atomic layer deposition. *J. Mater. Chem. A* **3**, 5360–5367 (2015). <https://doi.org/10.1039/c4ta06128d>
 44. Y. Yuan, J. Huang, Ion migration in organometal trihalide perovskite and its impact on photovoltaic efficiency and stability. *Acc. Chem. Res.* **49**(2), 286–293 (2016). <https://doi.org/10.1021/acs.accounts.5b00420>
 45. X. Yi, Z. Zhang, A. Chang, Y. Mao, Y. Luan et al., Incorporating CsF into the PbI_2 film for stable mixed cation-halide perovskite solar cells. *Adv. Energy Mater.* **9**, 1901726 (2019). <https://doi.org/10.1002/aenm.201901726>
 46. J. Yang, C. Liu, C. Cai, X. Hu, Z. Huang et al., High-performance perovskite solar cells with excellent humidity and thermo-stability via fluorinated perylene diimide. *Adv. Energy Mater.* **9**, 190019810 (2019). <https://doi.org/10.1002/aenm.201900198>
 47. R. Wang, J. Xue, L. Meng, J.-W. Lee, Z. Zhao et al., Caffeine improves the performance and thermal stability of perovskite solar cells. *Joule* **3**, 1464–1477 (2019). <https://doi.org/10.1016/j.joule.2019.04.005>
 48. L. Zhou, Z. Lin, Z. Ning, T. Li, X. Guo et al., Highly efficient and stable planar perovskite solar cells with modulated diffusion passivation toward high power conversion efficiency and ultrahigh fill factor. *Sol. RRL* **3**, 1900293 (2019). <https://doi.org/10.1002/solr.201900293>
 49. A. Guerrero, G. Garcia-Belmonte, I. Mora-Sero, J. Bisquert, Y.S. Kang et al., Properties of contact and bulk impedances in hybrid lead halide perovskite solar cells including inductive loop elements. *J. Phys. Chem. C* **120**(15), 8023–8032 (2016). <https://doi.org/10.1021/acs.jpcc.6b01728>
 50. S.R. Cowan, A. Roy, A.J. Heeger, Recombination in polymer-fullerene bulk heterojunction solar cells. *Phys. Rev. B* **82**, 245207 (2010). <https://doi.org/10.1103/PhysRevB.82.245207>
 51. J. Chen, Z. Wan, J. Liu, S.Q. Fu, F. Zhang et al., Growth of compact $\text{CH}_3\text{NH}_3\text{PbI}_3$ thin films governed by the crystallization in PbI_2 matrix for efficient planar perovskite solar cells. *ACS Appl. Mater. Interfaces* **10**(10), 8649–8658 (2018). <https://doi.org/10.1021/acsami.7b18667>
 52. Q. Dong, Y. Fang, Y. Shao, P. Mulligan, J. Qiu, L. Cao, J. Huang, Electron-hole diffusion lengths $> 175\ \mu\text{m}$ in solution-grown $\text{CH}_3\text{NH}_3\text{PbI}_3$ single crystals. *Science* **347**(6225), 967–970 (2015). <https://doi.org/10.1126/science.aaa5760>
 53. S.M. Ali, S.M. Ramay, M.H. Aziz, N. ur-Rehman, M.S. AlGarawi et al., Efficiency enhancement of perovskite solar cells by incorporation of CdS quantum dot through fast electron injection. *Org. Electron.* **62**, 21–25 (2018). <https://doi.org/10.1016/j.orgel.2018.07.012>
 54. P. Li, Y. Zhang, C. Liang, G. Xing, X. Liu et al., Phase pure 2D perovskite for high-performance 2D–3D heterostructured perovskite solar cells. *Adv. Mater.* **30**, 1805323 (2018). <https://doi.org/10.1002/adma.201805323>
 55. A.K.K. Kyaw, D.H. Wang, D. Wynands, J. Zhang, T.Q. Nguyen, G.C. Bazan, A.J. Heeger, Improved light harvesting and improved efficiency by insertion of an optical spacer (ZnO) in solution-processed small-molecule solar cells. *Nano Lett.* **13**(8), 3796–3801 (2013). <https://doi.org/10.1021/nl401758g>

56. H. Li, J. Cao, Q. Zhou, L. Ding, J. Wang, High-performance inverted PThTPTI: PC71BM solar cells. *Nano Energy* **15**, 125 (2015). <https://doi.org/10.1016/j.nanoen.2015.04.016s>
57. D. Bi, L. Yang, G. Boschloo, A. Hagfeldt, E.M.J. Johansson, Effect of different hole transport materials on recombination in $\text{CH}_3\text{NH}_3\text{PbI}_3$ perovskite-sensitized mesoscopic solar cells. *J. Phys. Chem. Lett.* **4**(9), 1532–1536 (2013). <https://doi.org/10.1021/jz400638x>
58. L.J.A. Koster, V.D. Mihailetschi, H. Xie, P.W.M. Blom, Origin of the light intensity dependence of the short-circuit current of polymer/fullerene solar cells. *Appl. Phys. Lett.* **87**, 203502 (2005). <https://doi.org/10.1063/1.2130396>
59. V.D. Mihailetschi, J. Wildeman, P.W.M. Blom, Space-charge limited photocurrent. *Phys. Rev. Lett.* **94**, 126602 (2005). <https://doi.org/10.1103/PhysRevLett.94.126602>
60. H. Li, Z.G. Zhang, Y. Li, J. Wang, Tunable open-circuit voltage in ternary organic solar cells. *Appl. Phys. Lett.* **101**, 163302 (2012). <https://doi.org/10.1063/1.4761246>
61. B. Qi, J. Wang, Open-circuit voltage in organic solar cells. *J. Mater. Chem.* **22**, 24315–24325 (2012). <https://doi.org/10.1039/C2JM33719C>
62. M.M. Mandoc, F.B. Kooistra, J.C. Hummelen, B. De Boer, P.W.M. Blom, Effect of traps on the performance of bulk heterojunction organic solar cells. *Appl. Phys. Lett.* **91**, 263505 (2007). <https://doi.org/10.1063/1.2821368>
63. S.R. Cowan, W.L. Leong, N. Banerji, G. Dennler, A.J. Heeger, Identifying a threshold impurity level for organic solar cells: enhanced first-order recombination via well-defined PC_{84}BM traps in organic bulk Heterojunction solar cells. *Adv. Funct. Mater.* **21**(16), 3083–3092 (2011). <https://doi.org/10.1039/C2JM33719C>

